entropy

IMPACT FACTOR 2.1

Indexed in: PubMed

CITESCORE 4.9

Article

Anomalous Behavior of the Non-Hermitian Topological System with an Asymmetric Coupling Impurity

Junjie Wang, Fude Li and Weijun Cheng

Special Issue

Entropy: From Atoms to Complex Systems

Edited by

Dr. Caroline Desgranges

MDPI

https://doi.org/10.3390/e27010078

entropy

MDPI

Article

Anomalous Behavior of the Non-Hermitian Topological System with an Asymmetric Coupling Impurity

Junjie Wang [1,*], Fude Li [2] and Weijun Cheng [3]

[1] College of Digital Technology and Engineering, Ningbo University of Finance & Economics, Ningbo 315175, China
[2] College of Computer and Information Engineering, Tianjin Agricultural University, Tianjin 300384, China; lifd283@nenu.edu.cn
[3] School of Integrated Circuits, Tsinghua University, Beijing 100084, China; chengwj177@nenu.edu.cn
* Correspondence: wangjj012@nenu.edu.cn

Abstract: A notable feature of systems with non-Hermitian skin effects is the sensitivity to boundary conditions. In this work, we introduce one type of boundary condition provided by a coupling impurity. We consider a system where a two-level system as an impurity couples to a nonreciprocal Su–Schrieffer–Heeger chain under periodic boundary conditions at two points with asymmetric couplings. We first study the spectrum of the system and find that asymmetric couplings lead to topological phase transitions. Meanwhile, a striking feature is that the coupling impurity can act as an effective boundary, and asymmetric couplings can also induce a flexibly adjusted zero mode. It is localized at one of the two effective boundaries or both of them by tuning coupling strengths. Moreover, we uncover three types of localization behaviors of eigenstates for this non-Hermitian impurity system with on-site disorder. These results corroborate the potential for control of a class of non-Hermitian systems with coupling impurities.

Keywords: impurity; non-Hermitian system; quantum phase transition

Academic Editor: Alessandro Cuccoli

Received: 7 December 2024
Revised: 8 January 2025
Accepted: 14 January 2025
Published: 17 January 2025

Citation: Wang, J.; Li, F.; Cheng, W. Anomalous Behavior of the Non-Hermitian Topological System with an Asymmetric Coupling Impurity. *Entropy* **2025**, *27*, 78. https://doi.org/10.3390/e27010078

1. Introduction

In recent years, non-Hermitian physics has attracted a plethora of attention, uncovering a wide range of phenomena and applications in both classical and quantum systems [1–37]. Non-Hermitian systems also exhibit some markedly different properties with no conventional Hermitian counterparts, such as biorthogonal eigenstates [2], exceptional points [5,6], and the breakdown of the conventional bulk–boundary correspondence [15–18].

Another unique feature of the non-Hermitian system is the accumulation of all eigenstates at the boundaries, which is a phenomenon dubbed the "non-Hermitian skin effect" [17]. A notable feature of systems with non-Hermitian skin effects is that the properties of both spectrum and eigenstates may be dramatically changed by turning the boundary conditions from periodic to open ones. In between, an impurity introduced into the system could also play the role of the boundary [38–45]. A striking feature of the impurity model is that boundary impurities can generate new types of steady-state localization behavior characterized by scale-free accumulation of eigenstates [38]. Due to the fact that the energy shift of the system can be extraordinarily changed by adding a vanishingly small boundary impurity, this kind of system can also be harnessed to devise sensors in an experimentally realistic setting [46–49].

Recently, simulations of topological systems using superconducting quantum circuits have attracted a great deal of attention [50–53]. On the other hand, superconducting qubits acting as giant artificial atoms have played an important role in superconducting quantum circuits. They can be nonlocally coupled to a waveguide at multiple points [54–59]. It was observed that the giant atom can act as an effective boundary and induce chiral zero modes for the waveguide in Hermitian topological systems [58,59].

These studies also further stimulate a new research direction for the interaction between the non-Hermitian topological system and quantum emitters [60–64]. In Ref. [63], the researchers found that giant emitters can exhibit essentially different dynamical behaviors by turning the relative strengths of the nonlocal couplings, and a series of unconventional quantum optical phenomena have been unveiled, such as nonreciprocal decoherence-free interaction. In Ref. [64], focusing on spectrum structures and the localization of eigenstates for the system that a giant atom as an impurity couples to a non-Hermitian topological chain with the same nonlocal coupling strengths, the authors mainly found that the impurity can induce asymmetric zero modes. This begs the question that what new physical phenomena will emerge in this type of systems by leveraging the relative strengths of the nonlocal couplings.

In this work, we focus on a system composed of a two-level system as an impurity and a nonreciprocal Su–Schrieffer–Heeger (SSH) chain with asymmetric couplings. We first study the fundamental properties of the spectrum and find that asymmetric couplings can cause topological phase transitions in an $A-B$ coupling case. As two coupling strengths g_n and g_m become more and more different, it seems that the zero mode will always exist. We further reveal the localization behaviors of zero mode for the system. It can be localized at one of the two effective boundaries or both of them depending on the relative strengths of the nonlocal couplings. We also show three types of localization behaviors of all eigenstates for systems with on-site disorder in the end.

The paper is organized as follows. In Section 2, we introduce a model to describe a system composed of a two-level system and a nonreciprocal SSH chain. In Section 3, firstly, we show the spectrum of the system, and we give the reason for the occurrence of topological phase transitions. Secondly, we derive analytical expressions and show numerical simulations for the zero modes. In the end, we introduce the mean center of mass (mcom) to describe the localization feature of all eigenstates with on-site disorder. In Section 4, we summarize our results.

2. Model and Methods

We consider a nonreciprocal SSH chain with the periodic boundary conditions (PBCs) in real space. The non-Hermitian Hamiltonian associated with this chain can be written as follows:

$$\begin{aligned} H_{\mathrm{SSH}} = \sum_{l=1}^{L} [&(t_1+\gamma)\hat{C}_{A,l}^{\dagger}\hat{C}_{B,l} + (t_1-\gamma)\hat{C}_{B,l}^{\dagger}\hat{C}_{A,l} \\ &+ t_2\hat{C}_{A,l+1}^{\dagger}\hat{C}_{B,l} + t_2\hat{C}_{B,l}^{\dagger}\hat{C}_{A,l+1}], \end{aligned} \tag{1}$$

where the chain is composed of L unit cells, with each containing two sites. $\hat{C}_{A(B),l}^{\dagger}$ and $\hat{C}_{A(B),l}$ are the creation and annihilation operators for the sublattice site $A(B)$ at the l-th unit cell. The parameters $t_1 \pm \gamma$ and t_2 are intracell and intercell couplings. The asymmetry of hopping amplitudes ($\gamma \neq 0$) leads to the non-Hermiticity of the system.

We here focus on analyzing what occurs when a two-level impurity couples to a nonreciprocal SSH chain with asymmetric coupling, as schematically shown in Figure 1. Hence, we introduce a two-level impurity coupling at two points to a nonreciprocal SSH chain via $A-B$ couplings [Figure 1a] or $A-A$ couplings [Figure 1b], where nonlocal

coupling points locate at n-th lattice site and m-th lattice site. The system with $B-B$ couplings and system with $A-A$ couplings are very similar, so we do not study the case with $B-B$ couplings. Without loss of generality, we hereafter assume $n<m$. The interaction Hamiltonian between the impurity and the nonreciprocal SSH chain is given as

$$\begin{aligned} H_{I,AB} &= g_n\sigma^+\hat{C}_{A,n} + g_m\sigma^+\hat{C}_{B,m} + \text{H.c.}, \\ H_{I,AA} &= g_n\sigma^+\hat{C}_{A,n} + g_m\sigma^+\hat{C}_{A,m} + \text{H.c.}, \end{aligned} \tag{2}$$

where $g_n(g_m)$ is the coupling strength between the impurity and the n-th (m-th) site of the nonreciprocal SSH chain. $\sigma^+ = |e\rangle\langle g|$ is the usual pseudospin ladder operator, and $|g\rangle$ and $|e\rangle$ are the ground state and the excited state of the impurity, respectively. The total Hamiltonians of the atom–chain coupling can be expressed as

$$H_{AB} = H_{\text{SSH}} + H_{I,AB}, \tag{3a}$$

$$H_{AA} = H_{\text{SSH}} + H_{I,AA}. \tag{3b}$$

We have assumed that the impurity is resonant with the energy band center, i.e., frequency of impurity is zero. For the particularly experimental scheme, adding a constant imaginary shift to all sites corresponding to a passive setting with loss only [65], this correction does not affect the localization of eigenstates or the existence of boundary modes.

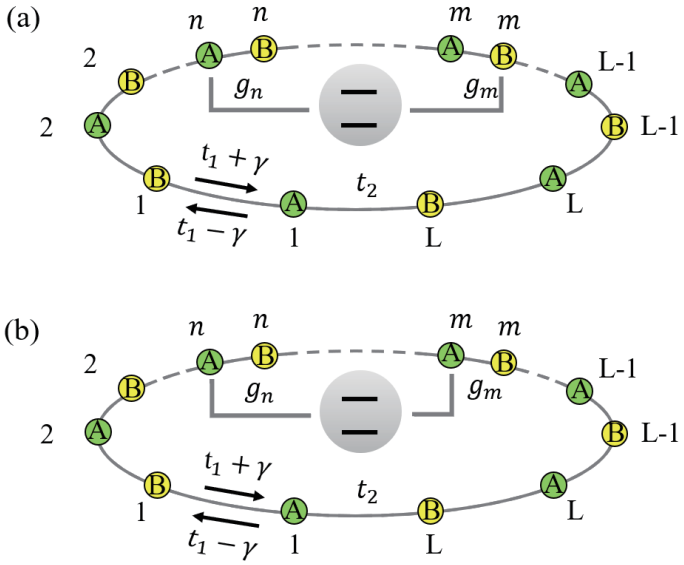

Figure 1. Schematicsof the nonreciprocal SSH chain coupled to an impurity via either $A-B$ coupling (**a**) or $A-A$ coupling (**b**) with asymmetric coupling strengths ($g_m \neq g_n$).

This model can be observed in a range of experimental settings, including electrical circuits [33,49] and photonic systems [46]. For example, there are $2L$ nodes in our designed non-Hermitian topological circuit. The intercell coupling of the circuit is fulfilled by a capacitor. The nonreciprocal coupling can be achieved through connecting capacitors in series with a voltage follower. Due to the virtual open and virtual short circuit conditions between the inverting input and noninverting input pins, the current at the one side of the capacitor is blocked, while it remains uninfluenced at the other side. Impurity can be realized by using Josephson junctions [66] or just a node in the circuit [49]. The coupling between the impurity and chain is achieved by connecting a capacitor. And then the variation of coupling strength can be achieved by adjusting the capacitance. In addition, this model can also be thought of as an array of coupled optical ring resonators [46]. The asymmetric coupling has been experimentally achieved by introducing two scatterers into

the mode volume of a ring resonator. The intercell coupling may be achieved by chiral couplers. The coupling between impurity and chain may be represented by any optically impenetrable region imposing a tunneling barrier. The variation of coupling strength then only needs to change the refractive index of the impenetrable medium.

3. Results

3.1. Spectrum and Topological Phase Transition

To illustrate the role of coupling impurity in the SSH chain. In Figure 2a, we first show the spectrum of pure SSH chain under periodic boundary conditions in the complex plane as a contrast. We also show spectrum of the system with $A-B$ couplings (3a) and $A-A$ couplings (3b) in Figure 2b,c, respectively. Note that an obvious feature is that the impurity can induce zero modes. This implies that the impurity can act as an effective boundary for a nonreciprocal SSH chain. Except for the zero modes, what are also called middle bound states, there are other eigenvalues outside the continuous bands. According to the value of the real part of the spectrum as a comparison, we call the corresponding eigenstates upper and lower bound states, respectively. The feature of these bound states will be described in the next section. Then, we study the spectrum feature of systems with $A-B$ couplings and $A-A$ couplings in detail.

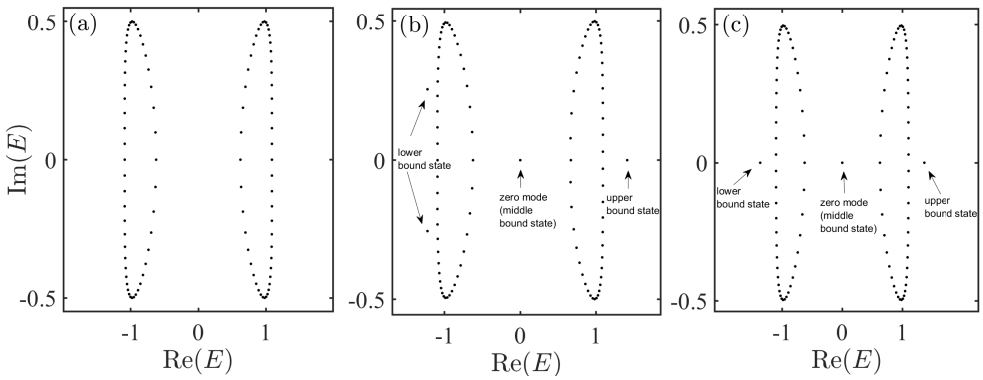

Figure 2. (**a**) Spectrum of pure SSH chain (1) in complex plane. (**b**) Spectrum of the system with $A-B$ couplings (3a) in complex plane. (**c**) Spectrum of the system with $A-A$ couplings (3b) in complex plane. The results were obtained by numerically solving the Schödinger equation. The parameters were set as $L=50, m=26, n=25, g_n=0.5, g_m=1, t_1=0.2, t_2=1$, and $\gamma=0.5$.

Firstly, for the $A-B$ coupling case (3a), we show the absolute value of the spectrum as a function of t_1 in Figure 3. The results were obtained by numerically solving the Schödinger equation. The asymmetric coupling strengths were set as $g_m=1$, $g_n=0.5$, 0.1, 0.01, and 0.001 for (a), (b), (c), and (d), respectively. In fact, the spectrum feature for the system with the same coupling strengths ($g_n=g_m=1$) has been studied in Ref. [64] in detail. A main finding is the condition for the emergence of the zero mode, i.e., $t_1\in[-t_2+\gamma, t_2-\gamma]$. In Figure 3a, one can see that the condition for the emergence of the zero mode in this case ($g_n=0.5$, $g_m=1$) is identical to the result with the same coupling strengths ($g_n=g_m=1$). However, this condition no longer holds as the two coupling strengths g_n and g_m become more and more different, as shown in Figure 3b–d. A striking feature is that when the coupling strength $g_n=0.001$ is much smaller than $g_m=1$, it seems that zero mode will always exist and not change with the parameters t_1, as shown in Figure 3d. This implies that asymmetric couplings can cause topological phase transitions.

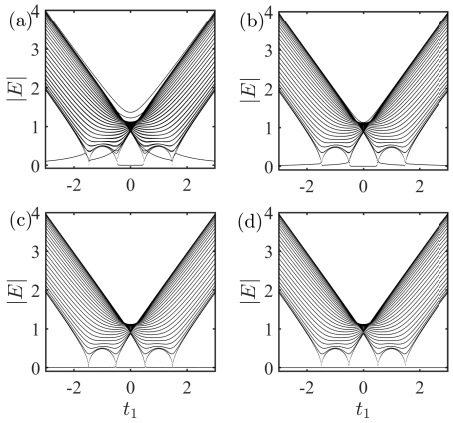

Figure 3. Absolute value of the spectrum as a function of t_1 with $A-B$ coupling. The results are obtained by numerically solve the Schödinger equation. $g_n = 0.5, 0.1, 0.01$, and 0.001 for (**a**), (**b**), (**c**), and (**d**), respectively. The other parameters were set as $L = 50, m = 26, n = 25, g_m = 1, t_2 = 1$, and $\gamma = 0.5$.

In order to derive a condition for the emergence of the zero mode and show why asymmetric couplings cause topological phase transitions, we first give the Hamiltonian of the system in the momentum space via Fourier transformation described by

$$\begin{aligned}\mathbb{H}_{AB}(k) =& \mathbb{H}_{\mathrm{SSH}}(k) + \mathbb{H}_{I,AB}(k) \\ =& \sum_k [[(t_1+\gamma) + t_2 e^{-ik}]\hat{\mathbb{C}}^\dagger_{A,k}\hat{\mathbb{C}}_{B,k} + [(t_1-\gamma) + t_2 e^{ik}]\hat{\mathbb{C}}^\dagger_{B,k}\hat{\mathbb{C}}_{A,k}] \\ &+ \frac{1}{\sqrt{L}}\sum_k [\sigma^+(g_n\hat{\mathbb{C}}_{A,k}e^{ikn} + g_m\hat{\mathbb{C}}_{B,k}e^{ikm}) + \text{ H.c. }],\end{aligned} \tag{4}$$

where $\hat{\mathbb{C}}^\dagger_{A(B),k}$ and $\hat{\mathbb{C}}_{A(B),k}$ denote the creation and annihilation operators for the sublattice site $A(B)$ at the k-th unit cell in the momentum space. In the single-excitation subspace, the eigenstates of the Hamiltonian $\mathbb{H}_{AB}(k)$ can be written as follows:

$$|\Psi\rangle = U_e|e,G\rangle + \sum_k \alpha_k \hat{\mathbb{C}}^\dagger_{A,k}|g,G\rangle + \sum_k \beta_k \hat{\mathbb{C}}^\dagger_{B,k}|g,G\rangle, \tag{5}$$

where $|G\rangle$ is the ground state of the SSH chain (vacuum state), and $|e(g),G\rangle = |e(g)\rangle|G\rangle$ can be used to form a complete base for the whole system. $\alpha_k(\beta_k)$ denotes the amplitude for the sublattice site $A(B)$ at the k-th unit cell, and U_e denotes the amplitude at site of the impurity. With the time-independent Schrödinger equation $\mathbb{H}_{AB}(k)|\psi\rangle = E|\psi\rangle$, the transcendental equation for the energy E can be expressed as (See Appendix A for analytical results)

$$\begin{aligned}E =& \frac{(g_n^2+g_m^2)}{L}\sum_k \frac{E}{E^2-\omega_k^2} + \frac{2g_ng_m}{L}\sum_k (t_1\cos[k(m-n)] \\ &- \gamma\sin[k(m-n)] + t_2\cos[k(m-n+1)])/(E^2-\omega_k^2)\end{aligned} \tag{6}$$

with

$$\omega_k = \sqrt{(t_1+\gamma+t_2e^{-ik})(t_1-\gamma+t_2e^{ik})}. \tag{7}$$

Setting $E = 0$, we can obtain a condition for the emergence of the zero mode, i.e., $t_1 \in [-t_2+\gamma, t_2-\gamma]$. (See Appendix A for analytical results and Figure 3a for numerical simulations). This confirms that the condition for the emergence of the zero mode with

asymmetric couplings is identical to the result with the same coupling strengths. However, as $g_n \to 0$ ($g_m \to 0$ is similar), Equation (6) can be simplified as

$$E = \frac{g_m^2}{L} \sum_k \frac{E}{E^2 - \omega_k^2}. \tag{8}$$

Evidently, $E = 0$ is always the solution of the Equation (8), which implies that there is always a zero mode in the systems. Hence, the topological phase transitions occur as two coupling strengths g_n and g_m become more and more different (see Figure 3a–d for numerical simulations). This can also be understood in terms of symmetry. The matrix form of the Hamiltonian $\mathbb{H}_{AB}(k)$ in the local site basis satisfies

$$\mathbb{H}_{AB}(k) = \begin{pmatrix} 0 & t_1 + \gamma + t_2 e^{-ik_1} & 0 & 0 & \dots & \frac{g_n e^{-ik_1 n}}{\sqrt{L}} \\ t_1 - \gamma + t_2 e^{ik_1} & 0 & 0 & 0 & \dots & \frac{g_m e^{-ik_1 m}}{\sqrt{L}} \\ 0 & 0 & 0 & t_1 + \gamma + t_2 e^{-ik_2} & \dots & \frac{g_n e^{-ik_2 n}}{\sqrt{L}} \\ 0 & 0 & t_1 - \gamma + t_2 e^{ik_2} & 0 & \dots & \frac{g_m e^{-ik_2 m}}{\sqrt{L}} \\ \dots & \dots & \dots & \dots & \dots & \dots \\ \frac{g_n e^{ik_1 n}}{\sqrt{L}} & \frac{g_m e^{ik_1 m}}{\sqrt{L}} & \frac{g_n e^{ik_2 n}}{\sqrt{L}} & \frac{g_m e^{ik_2 m}}{\sqrt{L}} & \dots & 0 \end{pmatrix}, \tag{9}$$

where the system has $2L$ lattice sites and one site for impurity. This matrix [Hamiltonian $\mathbb{H}_{AB}(k)$] is no longer a block diagonal matric, since the impurity couples to the SSH chain. Hence, the Hamiltonian cannot be written as the form of $\mathrm{d}\cdot\sigma$ as usual. As is known to all, a pure nonreciprocal SSH model has a chiral symmetry. The spectrum of a chiral symmetric Hamiltonian is symmetric. For any state with energy E, there is a chiral symmetric partner with energy $-E$. While this model with $A - B$ couplings does not preserve chiral symmetry. However, when $g_n = 0$ ($g_m = 0$ is similar), this system can still preserve a chiral symmetry $\Gamma^{-1}\mathbb{H}_{AB}(k)\Gamma = -\mathbb{H}_{AA}(k)$ with

$$\Gamma = \begin{pmatrix} 1 & 0 & 0 & 0 & \dots & 0 \\ 0 & -1 & 0 & 0 & \dots & 0 \\ 0 & 0 & 1 & 0 & \dots & 0 \\ 0 & 0 & 0 & -1 & \dots & 0 \\ \dots & \dots & \dots & \dots & \dots & \dots \\ 0 & 0 & 0 & 0 & \dots & 1 \end{pmatrix}. \tag{10}$$

For this system ($g_n = 0$) with an odd number of site basis, the zero mode obviously always exists.

Physically speaking, for $g_n = 0$ (or $g_m = 0$), this is like a small atom coupled to a nonreciprocal SSH chain. Here, for the qubit coupled to a waveguide at one point, we call it "small atom". In this case, except for the sublattice site B at the m-th unit cell coupled to the atom as an effective boundary, the other parts of the SSH chain are similar to a chain with a A site at both ends. For this kind of boundary condition, there is always a zero mode as usual. In a word, when g_n (or g_m) goes from a finite value to zero, topological phase transitions will be bound to happen.

Next, consider a system (3b) consisting of an impurity coupled to a nonreciprocal SSH chain via $A - A$ coupling. In Figure 4, we show absolute value of the spectrum as a function of t_1 with the same parameters as used in Figure 3. Note that there is always a zero mode in the gap for the $A - A$ coupling, and this result does not change with the coupling strength. The Hamiltonian of the system in momentum space via the Fourier transformation can be described by

$$\begin{aligned}\mathbb{H}_{AA}(k) =& \mathbb{H}_{\mathrm{SSH}}(k) + \mathbb{H}_{I,AA}(k) \\ =& \sum_k [[(t_1+\gamma) + t_2 e^{-ik}]\hat{\mathbb{C}}^{\dagger}_{A,k}\hat{\mathbb{C}}_{B,k} + [(t_1-\gamma) + t_2 e^{ik}]\hat{\mathbb{C}}^{\dagger}_{B,k}\hat{\mathbb{C}}_{A,k}] \\ &+ \frac{1}{\sqrt{L}}\sum_k [|e\rangle\langle g|\hat{\mathbb{C}}_{A,k}\left(g_n e^{ikn} + g_m e^{ikm}\right) + \mathrm{H.c.}].\end{aligned} \tag{11}$$

Similarly, the matrix form of Hamiltonian (3b) in the momentum space can be expressed as

$$\mathbb{H}_{AA}(k) = \begin{pmatrix} 0 & t_1+\gamma+t_2e^{-ik_1} & 0 & 0 & \dots & \frac{g_n e^{-ik_1 n}+g_m e^{-ik_1 m}}{\sqrt{L}} \\ t_1-\gamma+t_2e^{ik_1} & 0 & 0 & 0 & \dots & 0 \\ 0 & 0 & 0 & t_1+\gamma+t_2e^{-ik_2} & \dots & \frac{g_n e^{-ik_2 n}+g_m e^{-ik_2 m}}{\sqrt{L}} \\ 0 & 0 & t_1-\gamma+t_2e^{ik_2} & 0 & \dots & 0 \\ \dots & \dots & \dots & \dots & \dots & \dots \\ \frac{g_n e^{-ik_1 n}+g_m e^{-ik_1 m}}{\sqrt{L}} & 0 & \frac{g_n e^{-ik_2 n}+g_m e^{-ik_2 m}}{\sqrt{L}} & 0 & \dots & 0 \end{pmatrix}. \tag{12}$$

The corresponding transcendental equation for energy E satisfies (See Appendix A for analytical results)

$$E = \frac{1}{L}\sum_k \left(\frac{g_n^2 + g_m^2 + 2g_n g_m \cos[k(m-n)])}{E^2 - \omega_k^2}\right). \tag{13}$$

Obviously, $E = 0$ is always the solution of Equation (13), which can be seen in the numerical spectra of Hamiltonian H_{AA} (Figure 3a–d). Fortunately, this system always has a chiral symmetry $\sigma^{-1}\mathbb{H}_{AA}(k)\sigma = -\mathbb{H}_{AA}(k)$ with

$$\sigma = \begin{pmatrix} 1 & 0 & 0 & 0 & \dots & 0 \\ 0 & -1 & 0 & 0 & \dots & 0 \\ 0 & 0 & 1 & 0 & \dots & 0 \\ 0 & 0 & 0 & -1 & \dots & 0 \\ \dots & \dots & \dots & \dots & \dots & \dots \\ 0 & 0 & 0 & 0 & \dots & -1 \end{pmatrix}. \tag{14}$$

Even after setting $g_n = 0$ or $g_m = 0$, we find that chiral symmetry will not vanish. This further indicates that zero mode will always exist.

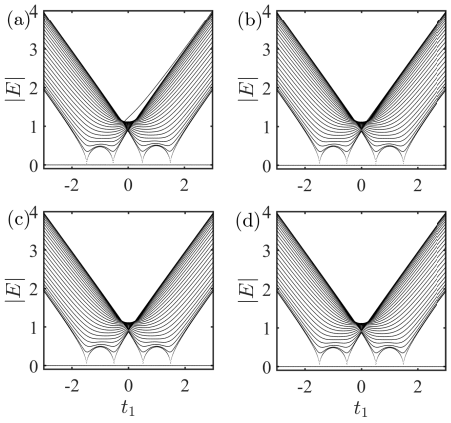

Figure 4. Absolute value of the spectrum as a function of t_1 with $A-A$ coupling. The results were obtained by numerically solving the Schödinger equation. $g_n = 0.5$, 0.1, 0.01, and 0.001 for (**a**), (**b**), (**c**), and (**d**), respectively. The other parameters were set as $L = 50, m = 26, n = 25, g_m = 1, t_2 = 1$, and $\gamma = 0.5$.

3.2. Localization of Zero Mode

In the previous section, we mainly found that asymmetric couplings can cause topological phase transitions for $A-B$ couplings. To illustrate this result again, we show the relationship between the localization of middle bound states and asymmetric couplings. To begin with, we define the population as modular square of the wave function $|\Psi_{A(B)}|^2$ in real space, and the populations of middle bound states for the system (3a) with $A-B$ coupling with different parameters g_n are shown in Figure 5a–d. Here, the parameters are $t_1=1$, $g_n=0.5$, 0.3, 0.1, and 0.01 for (a), (b), (c), and (d), respectively. The other parameters are the same as used in Figure 3a–d. One can see that middle bound states have no obvious symmetry for spatial distribution when $g_n=0.5$, as shown in Figure 5a. However, the spatial distribution of the bound state gradually becomes an exponential decay (type of zero mode) as g_n almost vanishes from a finite value, as shown in Figure 5d. This visually indicates that reducing one of the coupling strength can induce a zero mode.

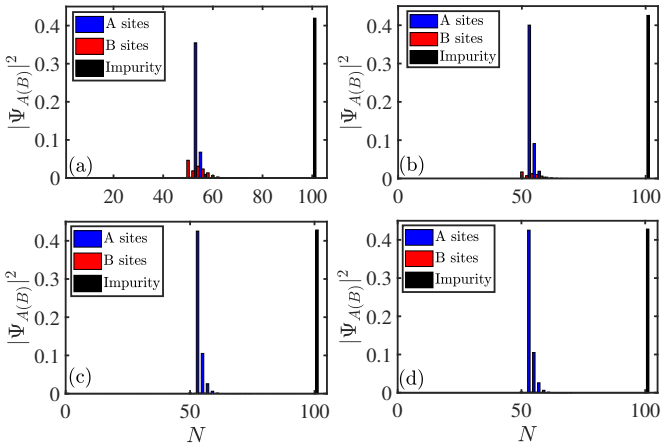

Figure 5. Populations of the middle bound states for the system (3a) with $A-B$ coupling as a function of site N. Here $g_n=0.5$, 0.3, 0.1, and 0.01 for (**a**), (**b**), (**c**), and (**d**), respectively. The other parameters were chosen as $L=50, m=26, n=25, g_m=1, t_1=1, t_2=1$, and $\gamma=0.5$. The site of impurity was set to $N=2L+1=101$.

Next, we are interested in analyzing localization of zero mode for the system wherein emitters couple to a nonreciprocal SSH chain. The populations of the zero mode as a function of site N with different parameters are shown in Figure 6 for $A-B$ coupling. The population on the impurity was set to $N=2L+1=101$. The bars represent numerical results and the empty circles represent the analytical results. The corresponding coefficients of wave function are as follows (See Appendix B for analytical results):

$$\begin{aligned} B_l/U_e &= \begin{cases} \frac{g_n}{t_1+\gamma}\left(-\frac{t_1+\gamma}{t_2}\right)^{(n-l)}, & (l<n), \\ 0, & (l\geq n), \end{cases} \\ A_l/U_e &= \begin{cases} 0, & (l\leq m), \\ \frac{g_m}{t_1-\gamma}\left(-\frac{t_1-\gamma}{t_2}\right)^{(l-m)}, & (l>m), \end{cases} \end{aligned} \tag{15}$$

where B_l (A_l) denotes the amplitude in the B(A) sublattice site of the l-th unit cell. Equation (15) shows that amplitudes in the wave function occupy B(A) lattice sites on the left (right) side of the impurity, and they satisfy exponential decay. Assuming $l=n-1$, we have $|B_{n-1}/U_e|=|g_n/t_2|$, and assuming $l=m+1$, we have $|A_{m+1}/U_e|=|g_m/t_2|$. This means that the zero modes mainly occupies B sites on the left side of the impurity when $g_n \gg g_m$ and occupies the A sites on the right side of the impurity when $g_m \gg g_n$. This has been clearly shown in Figure 6a–d. In addition, with the increase in $g_{n(m)}/t_2$, the

populations of zero mode on the impurity are gradually suppressed. This means that the spatial distribution of zero modes can be regulated by coupling strengths.

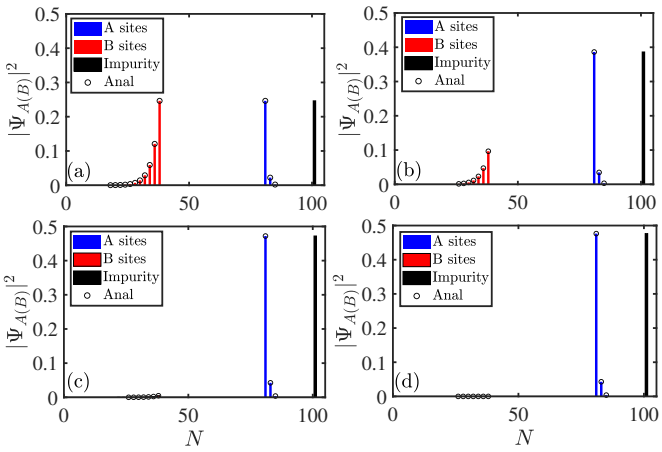

Figure 6. Populations of zero mode for the system (3a) with $A-B$ coupling as a function of site N. $g_n = 1, 0.5, 0.1$, and 0.01 for (**a**), (**b**), (**c**), and (**d**), respectively. The other parameters were chosen as $L = 50, m = 40, n = 20, g_m = 1, t_1 = 0.2, t_2 = 1$, and $\gamma = 0.5$. The site of impurity was set to $N = 2L + 1 = 101$.

For the system with $A-A$ coupling, zero modes always exist regardless of the value of parameters. Simple algebra (see Appendix B for analytical results) shows that amplitudes of zero modes take $A_l = 0$, and

$$B_l/U_e = \begin{cases} \frac{g_n}{t_1+\gamma}\left(\frac{-t_1-\gamma}{t_2}\right)^{(n-l)} + \frac{g_m}{t_1+\gamma}\left(\frac{-t_1-\gamma}{t_2}\right)^{(m-l)}, & (l<n), \\ \frac{g_m}{t_1+\gamma}\left(\frac{-t_1-\gamma}{t_2}\right)^{(m-l)}, & (n\le l<m), \\ 0, & (m\le l), \end{cases} \tag{16}$$

with $-t_2+\gamma < t_1 < t_2-\gamma$ and

$$B_l/U_e = \begin{cases} 0, & (l<n), \\ \frac{-g_n}{t_1+\gamma}\left(\frac{-t_2}{t_1+\gamma}\right)^{l-n}, & (n\le l<m), \\ \frac{-g_n}{t_1+\gamma}\left(\frac{-t_2}{t_1+\gamma}\right)^{l-n} + \frac{-g_m}{t_1+\gamma}\left(\frac{-t_2}{t_1+\gamma}\right)^{l-m}, & (m\le l), \end{cases} \tag{17}$$

with $t_1 > t_2+\gamma$ or $t_1 < -t_2-\gamma$. For $-t_2-\gamma < t_1 < -t_2+\gamma$ and $-t_2-\gamma < t_1 < -t_2+\gamma$, the analytical results of the zero mode are not given. Similarly, the spatial distribution of the zero modes can also be changed by tuning the coupling strengths g_m and g_n, as shown in Figure 7. It is clear that the analytical results (empty circles) given by Equation (16) are in good agreement with the numerical results (bars).

In this section, we mainly show that the localization of the zero modes is regulated by tuning the coupling strengths g_m and g_n for $A-B$ couplings and $A-A$ couplings. A notable feature is that the localization of the zero modes can be flexibly adjusted; as well, nonreciprocal hopping and asymmetric nonlocal couplings play a decisive role in systems. Concretely speaking, the impurity is nonlocally coupled to an SSH chain at two points and acts as two effective boundaries for the chain. Zero modes can localize at one of the two effective boundaries or both of them by tuning the coupling strengths g_m and g_n. While for a nonreciprocal SSH chain, zero modes only localize at one of the two boundaries due to the non-Hermitian skin effect. For Hermitian systems, zero modes localize at both the two boundaries. It is obviously seen that the localization of the the zero modes of these two systems is relatively fixed. In short, we find a zero mode that can be regulated

flexibly. In addition, except for the zero modes in the gap, there are other eigenvalues outside the continuous bands, as shown in Figure 3a. We call the corresponding eigenstates upper bound states. We find that these bound states can also be regulated by the coupling strengths g_m and g_n. See Appendix C for the analytical results and numerical simulations.

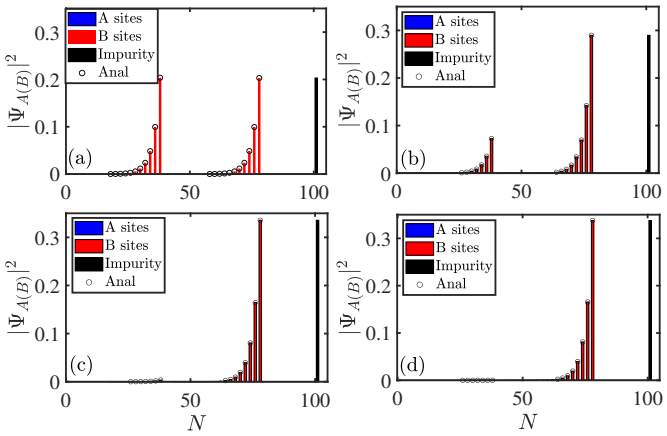

Figure 7. Population of zero mode for the system (3a) with $A-A$ coupling as a function of site N. $g_n = 1$, 0.5, 0.1, and 0.01 for (**a**), (**b**), (**c**), and (**d**), respectively. The other parameters were chosen as $L = 50, m = 40, n = 20, g_m = 1, t_1 = 0.2, t_2 = 1$, and $\gamma = 0.5$. The site of impurity was set to $N = 2L + 1 = 101$.

3.3. Systems with Disorder

We further explore the localization of all eigenstates for systems in the $A-A$ coupling case ($A-B$ couplings are similar) with on-site disorder. To this end, a Hamiltonian with disorder reads as

$$H_{\text{dis}} = H'_{\text{SSH}} + H_{I,AA}, \tag{18}$$

with

$$\begin{aligned} H'_{\text{SSH}} = \sum_{l=1}^{L} [&(t_1+\gamma_1)\hat{C}^{\dagger}_{A,l}\hat{C}_{B,l} + (t_1-\gamma_1)\hat{C}^{\dagger}_{B,l}\hat{C}_{A,l} \\ &+ t_2\hat{C}^{\dagger}_{A,l+1}\hat{C}_{B,l} + t_2\hat{C}^{\dagger}_{B,l}\hat{C}_{A,l+1} \\ &+ V_l\hat{C}^{\dagger}_{A,l}\hat{C}_{A,l} + V_l\hat{C}^{\dagger}_{B,l}\hat{C}_{B,l}] \end{aligned} \tag{19}$$

where V_l denotes an on-site disorder potential. Here, we set $V_l = SR_l$, where S is the disorder strength, and R_l is a normal random number.

This localization behavior of all eigenstates can be easily quantified by the mean center of mass (mcom) of the amplitude squared of all eigenvstates $|\Psi_{R,n}\rangle$ averaged over many disorder realizations as follows:

$$\text{mcom} = \frac{\sum_{\ell=1}^{N-1} \ell \langle \mathcal{A}(\ell) \rangle_V}{\sum_{\ell=1}^{N-1} \langle \mathcal{A}(\ell) \rangle_V}, \tag{20}$$

with

$$\langle \mathcal{A}(\ell) \rangle_V = \left\langle \frac{1}{N} \sum_{n=1}^{N} |\langle \ell \mid \Psi_{R,n} \rangle|^2 \right\rangle_V, \tag{21}$$

where $\langle \cdot \rangle_V$ indicates disorder averaging, and we are only interested in the wave functions living at the SSH chain, so the population of the impurity is not considered.

As shown in Figure 8, we plot the mcom as a function of coupling strength g_n and disorder strength S for the system with $A-A$ coupling. The results were averaged for 50 disorder realizations. Note that one can clearly see that in the limit of small disorder strength S and small coupling strength g_n, all eigenstates localize at the right coupling point

(white region in Figure 8). Thus, making the coupling strength g_n larger will gradually increase localization of the eigenstates to the left coupling point (black region in Figure 8). In addition, the system exhibits a different localization behavior with the increase in the disorder strength S. On-site potential disorder will always dominate, leading all eigenstates to localize on the basis of Anderson localization (red region in Figure 8). The localization behavior is that eigenstates are randomly localized at points in the SSH chain.

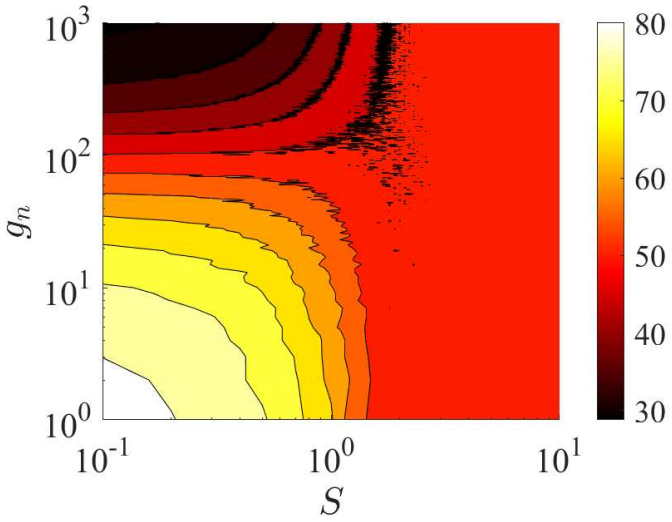

Figure 8. Mcom on the parameter space of coupling strengths g_n and disorder strengths S for the system with $A - A$ coupling. The results have been averaged for 50 disorder realizations. The parameters were chosen as $L = 50, m = 40, n = 10, g_m = 100, t_1 = 1, t_2 = 1$, and $\gamma = 0.5$. The site of impurity was set to $N = 2L + 1 = 101$.

4. Conclusions

In summary, we have studied an impurity coupled to a nonreciprocal SSH chain with asymmetric couplings. We show the fundamental properties of non-Hermitian spectra and find that asymmetric couplings can cause topological phase transitions for the $A - B$ couplings case. In addition, the interplay of asymmetric couplings and nonreciprocal hopping can induce flexibly adjusted zero modes. They are localized at one of the two effective boundaries or both of them by tuning the coupling strengths g_m and g_n. It is worth noting that the analytical results of the zero modes are precise and almost identify with the numerical results. We also explored the localization of all eigenstates for systems with on-site disorder, and we uncovered three types of localization behavior—localized at the right coupling point, localized at the left coupling point, and randomly localized at points in the SSH chain.

Author Contributions: Conceptualization, J.W.; Methodology, W.C.; Validation, F.L.; Writing—original draft, J.W.; Writing—review & editing, F.L. and W.C. All authors have read and agreed to the published version of the manuscript.

Funding: This work was supported by the National Natural Science Foundation of China (NSFC) under Grant No. 1240050250.

Data Availability Statement: The data are contained within the article.

Conflicts of Interest: The authors declare no conflicts of interest.

Appendix A. Energy Equation

Make use of the time-independent Schödinger equation $\mathbb{H}_{AB}(k)|\psi\rangle = E|\psi\rangle$, together with Equations (4) and (5) in the main text, which then leads to

$$\begin{aligned} EU_e &= \frac{1}{\sqrt{L}}\sum_k\Big(\alpha_k g_n e^{ikn} + \beta_k g_m e^{ikm}\Big), \\ E\alpha_k &= \Big(t_1 + \gamma + t_2 e^{-ik}\Big)\beta_k + \frac{g_n}{\sqrt{L}}e^{-ikn}U_e, \\ E\beta_k &= \Big(t_1 - \gamma + t_2 e^{ik}\Big)\alpha_k + \frac{g_m}{\sqrt{L}}e^{-ikm}U_e. \end{aligned} \tag{A1}$$

Eliminating α_k,β_k, and U_e from the above equations, we will obtain the transcendental equation for energy E as

$$\begin{aligned} E =& \frac{(g_n^2 + g_m^2)}{L}\sum_k \frac{E}{E^2 - \omega_k^2} + \frac{2g_n g_m}{L}\sum_k (t_1\cos[k(m-n)] \\ &- \gamma\sin[k(m-n)] + t_2\cos[k(m-n+1)])/(E^2 - \omega_k^2) \end{aligned} \tag{A2}$$

To discuss the existence condition of the zero mode, we set $E = 0$; then, Equation (A2) can be simplified as

$$\begin{aligned} 0 =& \frac{g_n g_m}{\pi}\int_{-\pi}^{\pi} dk(t_1\cos[k(m-n)] - \gamma\sin[k(m-n)] \\ &+ t_2\cos[k(m-n+1)])/(-\omega_k^2). \end{aligned} \tag{A3}$$

Simple algebra shows that the right-hand side of Equation (A3) = 0 when $t_1 \in [-t_2 + \gamma, t_2 - \gamma]$. This means that the condition for the emergence of the zero mode is $t_1 \in [-t_2 + \gamma, t_2 - \gamma]$.

Similarly, for the system with $A - A$ coupling, the Hamiltonian in the momentum space reads as

$$\begin{aligned} \mathbb{H}_{AA}(k) =& \mathbb{H}_{\mathrm{SSH}}(k) + \mathbb{H}_{I,AA}(k) \\ =& \sum_k [[(t_1 + \gamma) + t_2 e^{-ik}]\hat{\mathbb{C}}_{A,k}^{\dagger}\hat{\mathbb{C}}_{B,k} + [(t_1 - \gamma) + t_2 e^{ik}]\hat{\mathbb{C}}_{B,k}^{\dagger}\hat{\mathbb{C}}_{A,k}] \\ &+ \frac{1}{\sqrt{L}}\sum_k [|e\rangle\langle g|\hat{\mathbb{C}}_{A,k}\Big(g_n e^{ikn} + g_m e^{ikm}\Big) + \mathrm{H.c.}]. \end{aligned} \tag{A4}$$

$\mathbb{H}_{AA}(k)|\psi\rangle = E|\psi\rangle$ leads to

$$\begin{aligned} EU_e &= \frac{1}{\sqrt{L}}\sum_k \alpha_k\Big(g_n e^{ikn} + g_m e^{ikm}\Big), \\ E\alpha_k &= \Big(t_1 + \gamma + t_2 e^{-ik}\Big)\beta_k + \frac{1}{\sqrt{L}}\Big(g_n e^{-ikn} + g_m e^{-ikm}\Big)U_e, \\ E\beta_k &= \Big(t_1 - \gamma + t_2 e^{ik}\Big)\alpha_k. \end{aligned} \tag{A5}$$

Some algebraic calculations show that the energy E satisfies

$$E = \frac{1}{L}\sum_k\left(\frac{g_n^2 + g_m^2 + 2g_n g_m\cos[k(m-n)])}{E^2 - \omega_k^2}\right). \tag{A6}$$

Obviously, $E = 0$ is always the solution of the Equation (A6).

Appendix B. States outside the Band

For the system with $A-B$ couplings, according to the Equation (A1), amplitudes α_k and β_k satisfy

$$\begin{aligned}\alpha_k/U_e &= \frac{f(k)}{\sqrt{L}t_2}\left(g_n E e^{-ikn} + \left(t_1+\gamma+t_2e^{-ik}\right)g_m e^{-ikm}\right),\\ \beta_k/U_e &= \frac{f(k)}{\sqrt{L}t_2}\left(g_m E e^{-ikm} + \left(t_1-\delta+t_2e^{ik}\right)g_n e^{-ikn}\right),\end{aligned} \tag{A7}$$

where $f(k) = 1/(x-(t_1+\gamma)e^{ik}-(t_1-\gamma)e^{-ik})$, and $x = (E^2-(t_1+\gamma)(t_1-\gamma)-t_2^2)/t_2$. By Fourier expansion of $f(k)$, we will obtain the amplitude $A_l(B_l)$ in real space as follows:

$$\begin{aligned}A_l/U_e &= \frac{1}{\sqrt{L}}\sum_k e^{ikl}\alpha_k/U_e\\ &= \frac{(-1)^{y+1}\left(T\tau_1^{|l-n|}+g_m\tau_2^{|l-m-1|}+Y_2\tau_2^{|l-m|}\right)}{\sqrt{x^2-4(t_1+\gamma)(t_2-\gamma)}},\\ B_l/U_e &= \frac{1}{\sqrt{L}}\sum_k e^{ikl}\beta_k/U_e\\ &= \frac{(-1)^{y+1}\left(T\tau_2^{|l-m|}+g_n\tau_1^{|l-n+1|}+Y_1\tau_1^{|l-n|}\right)}{\sqrt{x^2-4(t_1+\gamma)(t_1-\gamma)}},\end{aligned} \tag{A8}$$

where $T = g_nE/t_2$, $Y_1 = g_n(t_1-\gamma)/t_2$, and $Y_2 = g_m(t_1+\gamma)/t_2$. In addition, $\tau_1 = a$ for $l \geq n$, and $\tau_1 = b$ for $l < n$. $\tau_2 = a$ for $l > m$, and $\tau_2 = b$ for $l \leq m$. And $a = (x+\sqrt{x^2-4(t_1+\gamma)(t_1-\gamma)})/2(t_1+\gamma), b = (x+\sqrt{x^2-4(t_1+\gamma)(t_1-\gamma)})/2(t_1-\gamma)$ for $x < -2|t_1|$ or $a = (x-\sqrt{x^2-4(t_1+\gamma)(t_1-\gamma)})/2(t_1+\gamma), b = (x-\sqrt{x^2-4(t_1+\gamma)(t_1-\gamma)})/2(t_1-\gamma)$ for $x > 2|t_1|$.

For the zero modes, setting $E = 0$, Equation (A8) can be simplified as

$$\begin{aligned}A_l/U_e &= \begin{cases}\frac{g_m}{t_1-\gamma}\left(-\frac{t_1-\gamma}{t_2}\right)^{(l-m)}, & (l>m),\\ 0, & (l\leq m),\end{cases}\\ B_l/U_e &= \begin{cases}\frac{g_n}{t_1+\gamma}\left(-\frac{t_1+\gamma}{t_2}\right)^{(n-l)}, & (l<n),\\ 0, & (l\geq n),\end{cases}\end{aligned} \tag{A9}$$

Similarly, for the system with $A-A$ coupling, Equation (A5) yields

$$\begin{aligned}\alpha_k/U_e &= \frac{E}{\sqrt{L}t_2}\left(g_n e^{-ikn}+g_m e^{-ikm}\right)f(k),\\ \beta_k/U_e &= \frac{\left(t_1-\gamma+t_2e^{ik}\right)}{\sqrt{L}t_2}\left(g_n e^{-ikn}+g_m e^{-ikm}\right)f(k).\end{aligned} \tag{A10}$$

Through the inverse Fourier transformation, we can obtain

$$
\begin{aligned}
A_l/U_e &= \frac{1}{\sqrt{L}}\sum_k e^{ikl}\alpha_k/U_e \\
&= \frac{(-1)^{y+1}T}{\sqrt{x^2-4(t_1+\gamma)(t_1-\gamma)}}\left(\tau_1^{|l-n|}+\tau_3^{|l-m|}\right), \\
B_l/U_e &= \frac{1}{\sqrt{L}}\sum_k e^{ikl}\beta_k/U_e \\
&= \frac{(-1)^{y+1}}{\sqrt{x^2-4(t_1+\gamma)(t_1-\gamma)}}\Big\{Y_1\left(\tau_1^{|l-n|}+\tau_3^{|l-m|}\right) \\
&+g\left(\tau_1^{|l-n+1|}+\tau_3^{|l-m+1|}\right)\Big\},
\end{aligned}
\tag{A11}
$$

where $\tau_3 = a$ for $l \geq m$, and $\tau_3 = b$ for $l < m$. Then by setting $E = 0$, Equation (A11) can be simplified as $A_l/U_e = 0$, where

$$
B_l/U_e = \begin{cases} 0, & (l<n), \\ \frac{-g_n}{t_1+\gamma}\left(\frac{-t_2}{t_1+\gamma}\right)^{l-n}, & (n\leq l<m), \\ \frac{-g_n}{t_1+\gamma}\left(\frac{-t_2}{t_1+\gamma}\right)^{l-n}+\frac{-g_m}{t_1+\gamma}\left(\frac{-t_2}{t_1+\gamma}\right)^{l-m}, & (m\leq l), \end{cases}
\tag{A12}
$$

for $t_1 > t_2+\gamma$ or $t_1 < -t_2-\gamma$, and

$$
B_l/U_e = \begin{cases} \frac{g_n}{t_1+\gamma}\left(\frac{-t_1-\gamma}{t_2}\right)^{(n-l)}+\frac{g_m}{t_1+\gamma}\left(\frac{-t_1-\gamma}{t_2}\right)^{(m-l)}, & (l<n), \\ \frac{g_m}{t_1+\gamma}\left(\frac{-t_1-\gamma}{t_2}\right)^{(m-l)}, & (n\leq l<m), \\ 0, & (m\leq l), \end{cases}
\tag{A13}
$$

for $-t_2+\gamma < t_1 < t_2-\gamma$.

Appendix C. Upper Bound States

In Figure A1a–d, we show the corresponding populations of the upper bound state with $A-B$ coupling and $A-A$ coupling, respectively. It is clearly shown that the analytical results (empty circles) given by Equations (A8) and (A11) are in good agreement with the numerical results (bars). The spatial distribution of the upper bound states can also be changed by tuning the coupling strengths g_m and g_n.

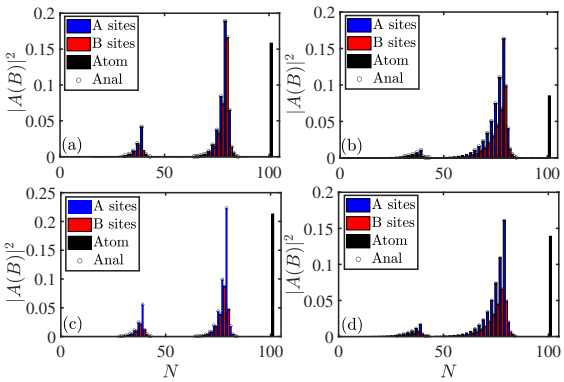

Figure A1. Populations of upper bound states in (**a**,**b**) with $A-B$ coupling and (**c**,**d**) with $A-A$ coupling as a function of site N. $g_n = 0.5$ for (**a**,**c**), and $g_n = 0.3$ for (**b**,**d**). The other parameters were chosen as $L = 50, m = 40, n = 20, g_m = 1, t_1 = 0.2, t_2 = 1$, and $\gamma = 0.5$. The site of impurity was set to $N = 2L+1 = 101$.

References

1. Moiseyev, N. *Non-Hermitian Quantum Mechanics*; Cambridge University Press: London, UK, 2011.
2. Brody, D.C. Biorthogonal quantum mechanics. *J. Phys. A Math. Theor.* **2013**, *47*, 035305. [CrossRef]
3. Ashida, Y.; Gong, Z.; Ueda, M. Non-Hermitian physics. *Adv. Phys.* **2020**, *69*, 249. [CrossRef]
4. Bergholtz, E.J.; Budich, J.C.; Kunst, F.K. Exceptional topology of non-Hermitian systems. *Rev. Mod. Phys.* **2021**, *93*, 015005. [CrossRef]
5. Berry, M.V. Physics of non-Hermitian degeneracies. *Czech. J. Phys.* **2004**, *54*, 1039. [CrossRef]
6. Heiss, W.D. The physics of exceptional points. *J. Phys. A Math. Theor.* **2012**, *45*, 444016. [CrossRef]
7. Liang, S.-D.; Huang, G.-Y. Topological invariance and global Berry phase in non-Hermitian systems. *Phys. Rev. A* **2013**, *87*, 012118. [CrossRef]
8. Lee, T.E. Anomalous edge state in a non-Hermitian lattice. *Phys. Rev. Lett.* **2016**, *116*, 133903. [CrossRef]
9. Leykam, D.; Bliokh, K.Y.; Huang, C.; Chong, Y.D.; Nori, F. Edge modes, degeneracies, and topological numbers in non-Hermitian systems. *Phys. Rev. Lett.* **2017**, *118*, 040401. [CrossRef] [PubMed]
10. Gong, Z.; Ashida, Y.; Kawabata, K.; Takasan, K.; Higashikawa, S.; Ueda, M. Topological phases of non-Hermitian systems. *Phys. Rev. X* **2018**, *8*, 031079.
11. Liu, T.; Zhang, Y.-R.; Ai, Q.; Gong, Z.P.; Kawabata, K.; Ueda, M.; Nori, F. Second-Order Topological Phases in Non-Hermitian Systems. *Phys. Rev. Lett.* **2019**, *122*, 076801. [CrossRef]
12. Yin, C.; Jiang, H.; Li, L.H.; Lü, R.; Chen, S. Geometrical meaning of winding number and its characterization of topological phases in one-dimensional chiral non-Hermitian systems. *Phys. Rev. A* **2018**, *97*, 052115. [CrossRef]
13. Lieu, S. Topological phases in the non-Hermitian Su-Schrieffer-Heeger model. *Phys. Rev. B* **2018**, *97*, 045106. [CrossRef]
14. Shen, H.; Zhen, B.; Fu, L. Topological band theory for non-Hermitian Hamiltonians. *Phys. Rev. Lett.* **2018**, *120*, 146402. [CrossRef]
15. Xiong, Y. Why does bulk boundary correspondence fail in some non-Hermitian topological models. *J. Phys. Commun.* **2018**, *2*, 035043. [CrossRef]
16. Kunst, F.K.; Edvardsson, E.; Budich, J.C.; Bergholtz, E.J. Biorthogonal Bulk-Boundary Correspondence in Non-Hermitian Systems. *Phys. Rev. Lett.* **2018**, *121*, 026808. [CrossRef] [PubMed]
17. Yao, S.Y.; Wang, Z. Edge States and topological invariants of non-Hermitian systems. *Phys. Rev. Lett.* **2018**, *121*, 086803. [CrossRef] [PubMed]
18. Yao, S.Y.; Song, F.; Wang, Z. Non-Hermitian Chern bands. *Phys. Rev. Lett.* **2018**, *121*, 136802. [CrossRef]
19. Song, F.; Yao, S.Y.; Wang, Z. Non-Hermitian Skin Effect and Chiral Damping in Open Quantum Systems. *Phys. Rev. Lett.* **2019**, *123*, 170401. [CrossRef]
20. Song, F.; Yao, S.Y.; Wang, Z. Non-Hermitian Topological Invariants in Real Space. *Phys. Rev. Lett.* **2019**, *123*, 246801. [CrossRef] [PubMed]
21. Yang, Z.S.; Zhang, K.; Fang, C.; Hu, J.P. Non-Hermitian Bulk-Boundary Correspondence and Auxiliary Generalized Brillouin Zone Theory. *Phys. Rev. Lett.* **2020**, *125*, 226402. [CrossRef] [PubMed]
22. Zhang, K.; Yang, Z.S.; Fang, C. Correspondence between Winding Numbers and Skin Modes in Non-Hermitian Systems. *Phys. Rev. Lett.* **2020**, *125*, 126402. [CrossRef]
23. Yi, Y.F.; Yang, Z.S. Non-Hermitian Skin Modes Induced by On-Site Dissipations and Chiral Tunneling Effect. *Phys. Rev. Lett.* **2020**, *125*, 186802. [CrossRef]
24. Okuma, N.; Kawabata, K.; Shiozaki, K.; Sato, M. Topological Origin of Non-Hermitian Skin Effects. *Phys. Rev. Lett.* **2020**, *124*, 086801. [CrossRef] [PubMed]
25. Borgnia, D.S.; Kruchkov, A.J.; Slager, R.-J. Non-Hermitian Boundary Modes and Topology. *Phys. Rev. Lett.* **2020**, *124*, 056802. [CrossRef]
26. Alvarez, V.M.M.; Vargas, J.E.B.; Torres, L.E.F.F. Non-Hermitian robust edge states in one dimension: Anomalous localization and eigenspace condensation at exceptional points. *Phys. Rev. B* **2018**, *97*, 121401. [CrossRef]
27. Lee, C.H.; Thomale, R. Anatomy of skin modes and topology in non-Hermitian systems. *Phys. Rev. B* **2019**, *99*, 201103. [CrossRef]
28. Li, L.H.; Lee, C.H.; Gong, J.B. Topological Switch for Non-Hermitian Skin Effect in Cold-Atom Systems with Loss. *Phys. Rev. Lett.* **2020**, *124*, 250402. [CrossRef] [PubMed]
29. Lee, C.H.; Li, L.H.; Gong, J.B. Hybrid Higher-Order Skin-Topological Modes in Nonreciprocal Systems. *Phys. Rev. Lett.* **2019**, *123*, 016805. [CrossRef]
30. Li, L.H.; Lee, C.H.; Mu, S.; Gong, J.B. Critical non-Hermitian skin effect. *Nat. Commun.* **2020**, *11*, 5491. [CrossRef]
31. Han, Y.Z.; Liu, J.S.; Liu, C.S. The topological counterparts of non-Hermitian SSH models. *New J. Phys.* **2021**, *23*, 123029. [CrossRef]
32. Banerjee, A.; Hegde, S.S.; Agarwala, A.; Narayan, A. Chiral metals and entrapped insulators in a one-dimensional topological non-Hermitian system. *Phys. Rev. B* **2022**, *105*, 205403. [CrossRef]
33. Liu, S.; Shao, R.; Ma, S.J.; Zhang, L.; You, O.; Wu, H.; Xiang, Y.J.; Cui, T.J.; Zhang, S. Non-Hermitian Skin Effect in a Non-Hermitian Electrical Circuit. *Research* **2021**, *9*, 5608038. [CrossRef] [PubMed]

34. Hofmann, T.; Helbig, T.; Schindler, F.; Salgo, N.; Brzezińska, M.; Greiter, M.; Kiessling, T.; Wolf, D.; Vollhardt, A.; Kabaši, A.; et al. Reciprocal skin effect and its realization in a topolectrical circuit. *Phys. Rev. Res.* **2020**, *2*, 023265. [CrossRef]
35. Xiao, L.; Deng, T.; Wang, K.; Zhu, G.; Wang, Z.; Yi, W.; Xue, P. Non-Hermitian bulk-boundary correspondence in quantum dynamics. *Nat. Phys.* **2020**, *16*, 761–766. [CrossRef]
36. Helbig, T.; Hofmann, T.; Imhof, S.; Abdelghany, M.; Kiessling, M.; Molenkamp, L.W.; Lee, C.H.; Szameit, A.; Greiter, M.; Thomale, R. Generalized bulk-boundary correspondence in non-Hermitian topolectrical circuits. *Nat. Phys.* **2020**, *16*, 747–750. [CrossRef]
37. Brandenbourger, M.; Locsin, X.; Lerner, E.; Coulais, C. Non-reciprocal robotic metamaterials. *Nat. Commun.* **2019**, *10*, 4608. [CrossRef] [PubMed]
38. Li, L.H.; Lee, C.H.; Gong, J.B. Impurity induced scale-free localization. *Commun. Phys.* **2021**, *4*, 42. [CrossRef]
39. Yokomizo, K.; Murakami, S. Scaling rule for the critical non-Hermitian skin effect. *Phys. Rev. B* **2021**, *104*, 165117. [CrossRef]
40. Guo, C.X.; Liu, C.H.; Zhao, X.M.; Liu, Y.X.; Chen, S. Exact Solution of Non-Hermitian Systems with Generalized Boundary Conditions: Size-Dependent Boundary Effect and Fragility of the Skin Effect. *Phys. Rev. Lett.* **2021**, *127*, 116801. [CrossRef]
41. Liu, Y.; Chen, S. Diagnosis of bulk phase diagram of nonreciprocal topological lattices by impurity modes. *Phys. Rev. B* **2020**, *102*, 075404. [CrossRef]
42. Roccati, F. Non-Hermitian skin effect as an impurity problem. *Phys. Rev. A* **2021**, *104*, 022215. [CrossRef]
43. Lu, J.; Shan, W.-Y.; Lu, H.-Z.; Shen, S.-Q. Non-magnetic impurities and in-gap bound states in topological insulators. *New J. Phys.* **2011**, *13*, 103016. [CrossRef]
44. Slager, R.-J.; Rademaker, L.; Zaanen, J.; Balents, L. Impurity-bound states and Green's function zeros as local signatures of topology. *Phys. Rev. B* **2015**, *92*, 085126. [CrossRef]
45. Molignini, P.; Arandes, O.; Bergholtz, E.J. Anomalous skin effects in disordered systems with a single non-Hermitian impurity. *Phys. Rev. Res.* **2023**, *5*, 033058. [CrossRef]
46. Budich, J.C.; Bergholtz, E.J. Non-Hermitian Topological Sensors. *Phys. Rev. Lett.* **2020**, *125*, 180403. [CrossRef] [PubMed]
47. McDonald, A.; Clerk, A.A. Exponentially-enhanced quantum sensing with non-Hermitian lattice dynamics. *Nat. Commun.* **2020**, *11*, 5382. [CrossRef]
48. Koch, F.; Budich, J.C. Quantum non-Hermitian topological sensors. *Phys. Rev. Res.* **2022**, *4*, 013113. [CrossRef]
49. Yuan, H.; Zhang, W.X.; Zhou, Z.L.; Wang, W.L.; Pan, N.Q.; Feng, Y.; Sun, H.J.; Zhang, X.D. Non-Hermitian topolectrical circuit sensor with high sensitivity. *Adv. Sci.* **2023**, *10*, 2301128. [CrossRef]
50. Schroer, M.D.; Kolodrubetz, M.H.; Kindel, W.F.; Sandberg, M.; Gao, J.; Vissers, M.R.; Pappas, D.P.; Polkovnikov, A.; Lehnert, K.W. Measuring a Topological Transition in an Artificial Spin-1/2 System. *Phys. Rev. Lett.* **2014**, *113*, 050402. [CrossRef]
51. Tao, Z.Y.; Yan, T.X.; Liu, W.Y.; Niu, J.J.; Zhou, Y.X.; Zhang, L.B.; Jia, H.; Chen, W.Q.; Liu, S.; Chen, Y.Z.; et al. Simulation of a topological phase transition in a kitaev chain with long-range coupling using a superconducting circuit. *Phys. Rev. B* **2020**, *101*, 035109. [CrossRef]
52. Flurin, E.; Ramasesh, V.V.; Hacohen-Gourgy, S.; Martin, L.S.; Yao, N.Y.; Siddiqi, I. Observing Topological Invariants Using Quantum Walks in Superconducting Circuits. *Phys. Rev. X* **2017**, *7*, 031023. [CrossRef]
53. Tan, X.S.; Zhang, D.W.; Liu, Q.; Xue, G.M.; Yu, H.F.; Zhu, Y.Q.; Yan, H.; Zhu, S.L.; Yu, Y. Topological Maxwell Metal Bands in a Superconducting Qutrit. *Phys. Rev. Lett.* **2018**, *120*, 130503. [CrossRef] [PubMed]
54. Kannan, B.; Ruckriegel, M.J.; Campbell, D.L.; Kockum, A.F.; Braumüller, J.; Kim, D.K.; Kjaergaard, M.; Krantz, P.; Melville, A.; Niedzielski, B.M.; et al. Waveguide quantum electrodynamics with superconducting artificial giant atoms. *Nature* **2020**, *583*, 775. [CrossRef]
55. Manenti, R.; Kockum, A.F.; Patterson, A.; Behrle, T.; Rahamim, J.; Tancredi, G.; Nori, F.; Leek, P.J. Circuit quantum acoustodynamics with surface acoustic waves. *Nat. Commun.* **2017**, *8*, 975. [CrossRef]
56. Sletten, L.R.; Moores, B.A.; Viennot, J.J.; Lehnert, K.W. Resolving Phonon Fock States in a Multimode Cavity with a Double-Slit Qubit. *Phys. Rev. X* **2019**, *9*, 021056. [CrossRef]
57. Wang, X.; Gao, Z.-M.; Li, J.-Q.; Zhu, H.B.; Li, H.-R. Unconventional quantum electrodynamics with a Hofstadter-ladder waveguide. *Phys. Rev. A* **2022**, *106*, 043703. [CrossRef]
58. Wang, X.; Liu, T.; Kockum, A.F.; Li, H.R.; Nori, F. Tunable Chiral Bound States with Giant Atoms. *Phys. Rev. Lett.* **2021**, *126*, 043602. [CrossRef]
59. Cheng, W.J.; Wang, Z.H.; Liu, Y.X. Topology and retardation effect of a giant atom in a topological waveguide. *Phys. Rev. A* **2022**, *106*, 033522. [CrossRef]
60. Roccati, F.; Lorenzo, S.; Calajo, G.; Palma, G.M.; Carollo, A.; Ciccarello, F. Exotic interactions mediated by a non-Hermitian photonic bath. *Optica* **2022**, *9*, 565–571. [CrossRef]
61. Gong, Z.; Bello, M.; Malz, D.; Kunst, F.K. Anomalous behaviors of quantum emitters in non-Hermitian baths. *Phys. Rev. Lett.* **2022**, *129*, 223601. [CrossRef] [PubMed]
62. Gong, Z.; Bello, M.; Malz, D.; Kunst, F.K. Bound states and photon emission in non-Hermitian nanophotonics. *Phys. Rev. A* **2022**, *106*, 053517. [CrossRef]

63. Du, L.; Guo, L.Z.; Zhang, Y.; Kockum, A.F. Giant emitters in a structured bath with non-Hermitian skin effect. *Phys. Rev. Res.* **2023**, *5*, L042040. [CrossRef]
64. Wang, J.J.; Li, F.D.; Yi, X.X. Giant atom induced zero modes and localization in the nonreciprocal Su-Schrieffer-Heeger chain. *J. Phys. A Math. Theor.* **2023**, *56*, 455306. [CrossRef]
65. Weimann, S.; Kremer, M.; Plotnik, Y.; Lumer, Y.; Nolte, S.; Makris, K.G.; Segev, M.; Rechtsman, M.C.; Szameit, A. Topologically protected bound states in photonic parity-time-symmetric crystals. *Nat. Mater.* **2017**, *16*, 433. [CrossRef] [PubMed]
66. Blais, A.; Grimsmo, A.L.; Girvin, S.M.; Wallraff, A. Circuit quantum electrodynamics. *Rev. Mod. Phys.* **2021**, *93*, 025005. [CrossRef]